RSC Advances

PAPER

View Article Online
View Journal | View Issue

Cite this: *RSC Adv.*, 2026, **16**, 26847

Sustainable strawberry DNA-based biomimetic interphase with synergistic buffering and directional transport for dendrite-free lithium metal batteries

Zeyang Xu, †[ab] Shanshan Song †[ab] and Ming He *[a]

Circumventing the environmental toxicity and high costs inherent in traditional animal-derived DNA extraction, this study pioneers a green farm to battery strategy utilizing high-yield biomass DNA obtained from octoploid strawberries *via* a non-toxic process. Based on this approach, we construct a biomimetic Cu@DNA interface that operates through a dual mechanism of molecular buffering and directional transport. Mechanistically, theoretical calculations reveal that the negatively charged phosphate backbone possesses a high binding energy of −7.13 eV, functioning as an electrostatic potential well to homogenize Li^+ flux and serving as a molecular buffer to effectively suppress dendrite growth. Simultaneously, the guanine/adenine base pairs, characterized by moderate binding energies (−2.77 eV and −1.61 eV), act as "stepping stones" to facilitate rapid Li^+ desolvation through transient nitrogen coordination, which directs ion transport and significantly enhances reaction kinetics. As a result, this synergistic effect lowers the nucleation overpotential by 51.4%, dropping from 0.1611 V to 0.0828 V, and enables ultra-stable symmetric cell cycling for 700 hours with a low hysteresis of 22 mV. Furthermore, the full cell exhibits superior rate capability with a discharge capacity of 130 mAh g^{-1} at 3C, maintaining 92.7% capacity retention after 300 cycles. Validating practical viability, pouch cells with a high cathode loading of 5 mg cm^{-2} achieve 500 stable cycles with a coulombic efficiency near 100%. Beyond elucidating the synergistic mechanism of DNA-Li^+ interactions, this work highlights the immense potential of agricultural biomass in sustainable high-energy batteries.

Received 22nd March 2026
Accepted 25th April 2026

DOI: 10.1039/d6ra02347a

rsc.li/rsc-advances

1 Introduction

With the advancement of global carbon neutrality goals and the explosive growth of the electric vehicle market, the development of high-energy-density energy storage systems has become an urgent priority.[1] Lithium metal batteries (LMBs), owing to the extremely high theoretical specific capacity (3860 mAh g^{-1}) and the lowest electrochemical potential (−3.040 V *vs.* SHE) of the lithium metal anode, are regarded as the most promising candidates for next generation high-energy batteries.[2,3] However, the commercialization of lithium metal anodes faces severe challenges at the interface, primarily including uncontrolled dendrite growth and unstable solid electrolyte interphase (SEI). During repeated charge/discharge cycles, microscopic irregularities on the copper current collector surface lead to uneven local current density distribution, inducing tip-preferred deposition of lithium ions and subsequently forming uncontrollable lithium dendrites.[4] These dendrites result in separator penetration with risk of thermal runaway, and also lead to the accumulation of "dead lithium" and the continuous consumption of active lithium sources.[5,6] Additionally, side reactions between highly active lithium metal and the electrolyte generate a structurally fragile and non-uniform solid electrolyte interphase (SEI) film, causing a sharp decline in coulombic efficiency (CE).[7]

Centered on these severe interfacial challenges, the academic community has proposed various strategies. The primary approach involves regulating the solvation structure of the electrolyte to stabilize the interface and enhance coulombic efficiency.[8,9] Another effective strategy is to construct lithiophilic three-dimensional host frameworks with high specific surface areas, which reduces local current density, thereby mitigating volume expansion and suppressing dendrite growth.[10] Beyond bulk-phase modification, the construction of artificial solid electrolyte interface with ion rectification and physical barrier functions has been demonstrated to guide uniform lithium deposition and significantly extend cycle life.[11] Among these approaches, constructing an ultra-thin artificial interface layer with high ionic conductivity on the current collector surface is deemed a simple and effective strategy. In

[a]*Electronic and Information Engineering Institute, Guang'an Institute of Technology, Guang'an, China. E-mail: heming_mail@163.com*
[b]*Electronic Engineering Institute, Chengdu Technological University, Chengdu, China*
† Equal contribution to the paper.

recent years, based on the sustainable development concept of green chemistry, natural biological macromolecules such as cellulose, silk fibroin, and DNA have shown great potential in the field of advanced battery materials due to their unique molecular structures, abundant polar functional groups, and environmental friendliness.[12,13] Specifically, DNA with precise double-helix structure and negatively charged phosphate backbone, can function as a "molecular guide rail" to guide cations and accomplish ion rectification. While the nitrogen and oxygen atoms rich in base pairs can act as lithiophilic sites to regulate the nucleation barrier. Mitta *et al.* reported the excellent performance of a gel electrolyte based on genomic DNA from biological species in electrochemical energy storage.[14] Ouyang *et al.* employed a DNA interface layer to effectively resolve the long-standing bottlenecks of anode-free lithium metal batteries.[15] Although these researches have utilized DNA to improve battery performance, their DNA sources mainly rely on animal-derived DNA (*e.g.*, salmon testes), and the extraction process often involves toxic organic solvents like phenol-chloroform, resulting in conflicting with the low-cost and environmental protection demands of large-scale energy storage.[16,17] In contrast, commercially cultivated plant strawberry belongs to an octoploid species,[18,19]and the DNA content in its cell nucleus is far higher than that of ordinary diploid organisms, offering an extremely high extraction yield.

In order to resolve the limitations of traditional animal-derived DNA and inspired by the precise recognition and self-assembly characteristics of biological molecules, this study innovatively employs plant-derived strawberry DNA to construct a biomimetic electrode interface (Cu@DNA) for lithium metal batteries. An efficient Li^+ regulatory network was constructed using the unique double-helix of strawberry DNA. Its dual-function design combines the "molecular buffering" effect achieved through ion pre-enrichment by the phosphate backbone and the "directional transport" capability enabled by transient Li–N coordination from nucleobase pairs, which together facilitate uniform two-dimensional lithium deposition. Crucially, this mechanism is rigorously validated by density functional theory (DFT) calculations, which establish a functional hierarchy governed by the distinct binding affinities of DNA segments: the phosphate backbone acts as a strong anchor to immobilize active Li species, while nucleobases serve as moderate-affinity pathways to accelerate ion migration.

The extraction of strawberry DNA is entirely green, using only a simple salt-alcohol precipitation method to efficiently obtain DNA from agricultural biomass without toxic reagents.[20] Experimental results show that this biomimetic interface significantly improves the cycle life and rate performance of coin cells and achieves 500 stable cycles in high-loading (5 mg cm^{-2}) pouch cells, demonstrating excellent potential for practical utilization.

2 Results and discussion

2.1 Fabrication of biomimetic DNA interface and battery assembly

In this study, biomass DNA was extracted from strawberries using a phase separation method. Strawberry tissues were ground and homogenized, and DNA was released in a lysis buffer containing NaCl and detergents. Subsequently, white fibrous DNA aggregates were precipitated by induction with cold ethanol (95%). The purified DNA was washed, dried, ground, and ultrasonically dispersed in a Tris–HCL buffer solution (pH 8.5) to prepare a homogeneous solution of 2 mg mL^{-1}. Then, using a precision drop-casting method, 5 mL of the DNA solution was coated onto the surface of polished and cleaned copper foil (10 cm × 10 cm). After standing at room temperature and then curing at 40 °C for 6 hours, the Cu@DNA biomimetic interface electrode was obtained. The fabrication process is illustrated in Fig. 1.

The Cu foil and the dried Cu@DNA were cut into disks with a diameter of 15 mm. In an argon-filled glove box (with H_2O and O_2 concentrations below 0.1 ppm), they were assembled with

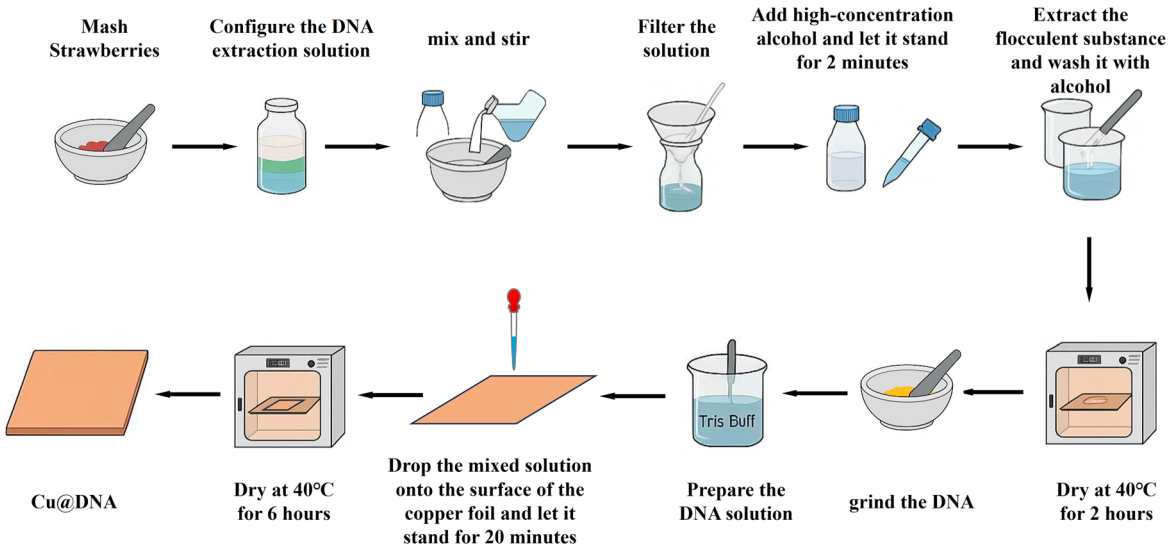

Fig. 1 Preparation process of extracted strawberry DNA molecules.

Φ12 mm lithium disks into Li|Cu and Li|Cu@DNA half-cells. The electrolyte utilized was 1.0 M $LiPF_6$ dissolved in a mixture of ethylene carbonate (EC) and diethyl carbonate (DEC) (1 : 1 v/v) with 5.0 wt% fluoroethylene carbonate (FEC) as a film-forming additive. A Celgard 2500 polypropylene membrane was used as the separator, and a constant volume of 40 μL of electrolyte was added to each CR2032 coin cell to ensure consistent wetting conditions. Cu and Cu@DNA were assembled with NCM811 into Cu|NCM811 and Cu@DNA|NCM811 full cells, respectively.

2.2 Theoretical calculations and mechanism analysis

To fundamentally elucidate the synergistic regulation mechanism of the Cu@DNA interface on Li^+ kinetics, density functional theory (DFT) calculations were performed using the Gaussian 16 software package. All molecular geometries were fully optimized using the B3LYP hybrid functional with the 6-31G(d,p) basis set. To provide a more accurate description of the non-covalent interactions, Grimme's D3 empirical dispersion correction was incorporated. Frequency analyses were carried out at the same level of theory to ensure that the optimized structures corresponded to local energy minima. The binding energy (E_b) was determined using the equation: $E_b = E_{total} - (E_{DNA} + E_{Li})$, where E_{total}, E_{DNA}, and E_{Li} are the electronic energies of the Li-adsorbed DNA fragment, the isolated DNA segment, and a single Li atom, respectively. The electrostatic potential (ESP) mappings Fig. 2(a), (c) and (e) visually reveal the charge distribution differences among the DNA functional units. The phosphate backbone exhibits a broad and intense electronegative region (red areas) around the oxygen atoms, with a minimum electrostatic potential reaching −0.203 a. u. In contrast, the electronegative regions of guanine (−0.087 a. u.) and adenine (−0.067 a. u.) are relatively localized around the N/O heteroatoms. According to the electrostatic interaction principle, the phosphate backbone with high negative charge density serves as a "super-lithiophilic" site.[21,22] This confirms its role as an "electrostatic potential well", which can effectively attract and pre-concentrate Li^+ from the bulk electrolyte, homogenizing the local ion flux distribution before deposition.[23]

Furthermore, the specific interaction strengths were quantified by calculating the binding energies (E_b) between Li and different DNA segments. As shown in Fig. 2(b), (d) and (f) the phosphate backbone exhibits the strongest binding affinity with an ultra-high E_b of −7.13 eV, significantly surpassing that of guanine (−2.77 eV) and adenine (−1.61 eV). This drastic energy difference establishes a functional hierarchy within the DNA molecule. Specifically, the phosphate backbone acts as a robust anchor to immobilize active Li species and suppress concentration polarization, effectively validating the 'Molecular Buffering' effect.[15] Simultaneously, the nucleobases (G/A), characterized by moderate binding energies, serve as 'stepping stones' for ion migration. Their interaction strength is strategically balanced—sufficient to strip the solvation sheath of Li^+ for desolvation, yet not strong enough to permanently trap the ions.[11] This resulting energy gradient facilitates the hopping of Li^+ along the N/O sites of the base pairs, realizing efficient 'Directional Transport' and accelerating reaction kinetics.[24] Consequently, the synergistic cooperation between the strong-adsorption backbone and moderate-adsorption bases ensures stable, dendrite-free lithium plating.

2.3 Microscopic and spectroscopic analysis

To visually investigate the microscopic morphological evolution of the electrode surface before and after modification, scanning electron microscopy (SEM) characterization was performed. As shown in Fig. 3(a), the bare copper foil exhibits a rough surface

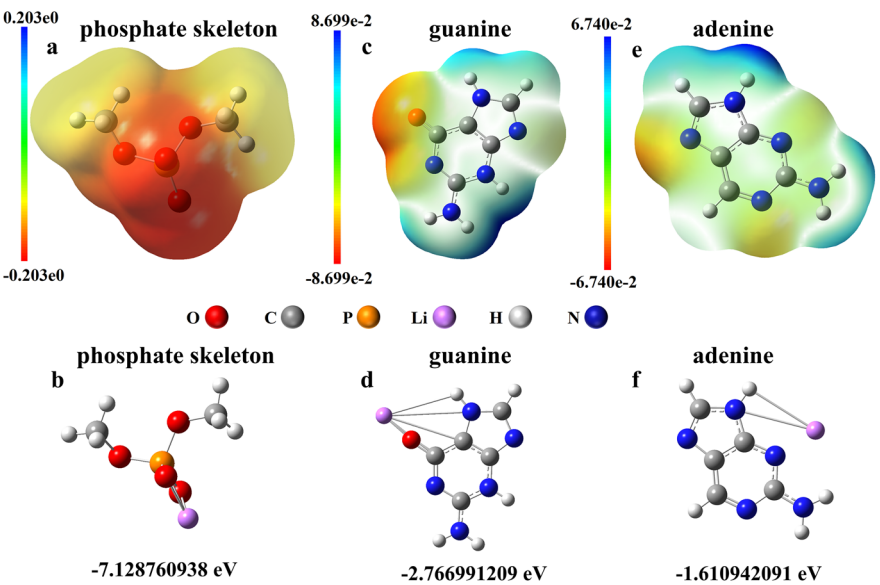

Fig. 2 Density functional theory (DFT) calculations of the interactions between Li^+ and DNA fragments. (a, c and e) Electrostatic potential (ESP) mapped molecular surfaces of the phosphate backbone, guanine, and adenine, respectively. The color scale ranges from red (negative potential) to blue (positive potential). (b, d and f) Optimized adsorption configurations and corresponding binding energies E_b of Li atom with the phosphate backbone, guanine, and adenine.

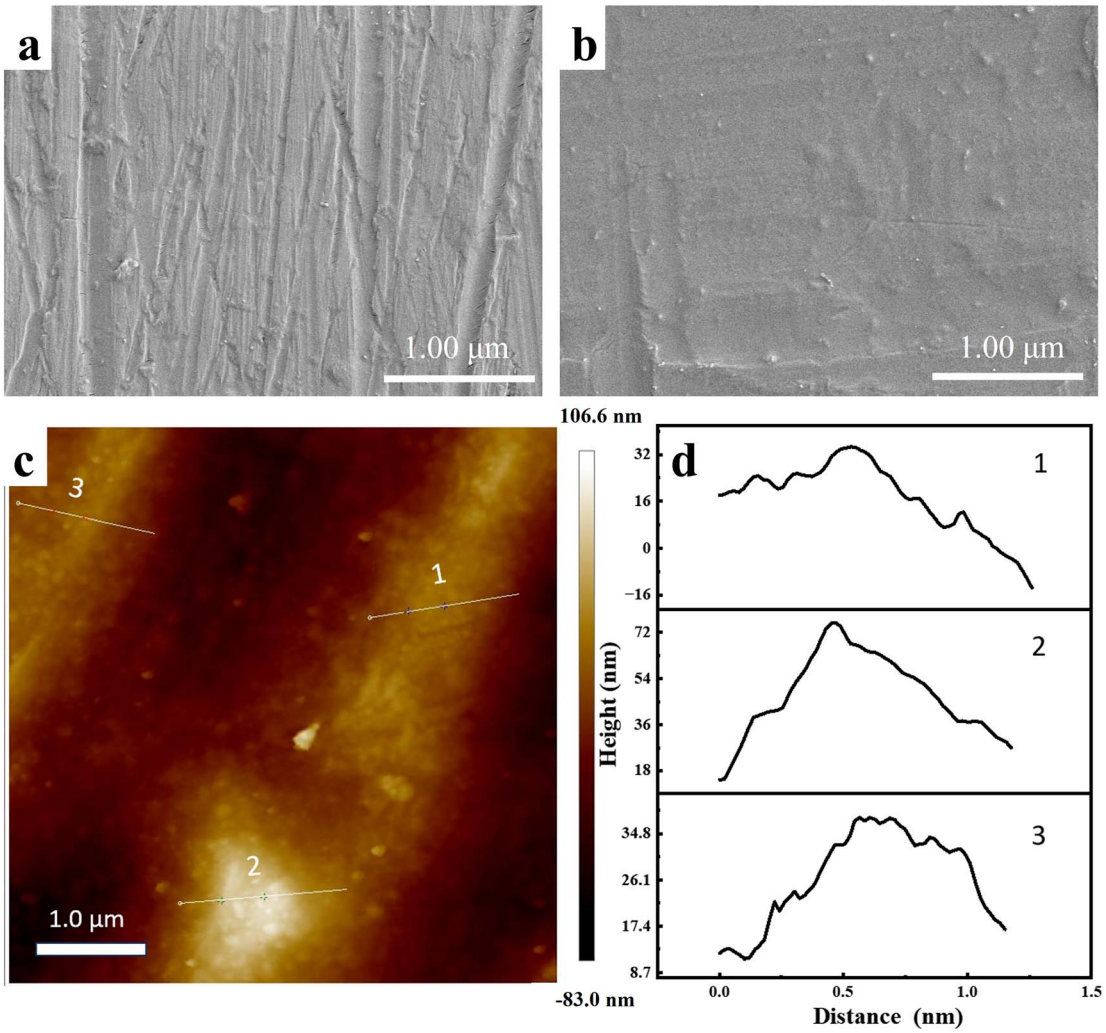

Fig. 3 Surface morphology characterization. Top-view SEM images of (a) bare Cu and (b) the Cu@DNA coating layer. (c) Atomic force microscopy (AFM) topography of the Cu@DNA surface, (d) Corresponding height profiles extracted from the lines in (c).

with abundant mechanical grooves and scratches derived from the manufacturing process. These microscopic defects often exacerbate electric field concentration, becoming "hotspots" for dendrite growth.[25] In contrast, the modified Cu@DNA surface presents a smooth, continuous, and semi-transparent film (Fig. 3(b)). It indicates that the DNA molecules have achieved conformal coverage on the copper substrate, effectively shielding the original surface defects. Atomic force microscopy (AFM) was further employed to analyze the surface topology. The 2D topography image in Fig. 3(c) reveals that the Cu@DNA layer possesses a unique, uniform nano-island texture rather than a completely flat surface. To quantitatively evaluate this microstructure, height profiles in Fig. 3(c) corresponding to the three representative scanning paths (labeled 1, 2, and 3) are plotted in Fig. 3(d). These curves consistently show regular height fluctuations (approx. 20–60 nm), confirming the uniform distribution of the DNA nano-domains. This specific nano-texture is beneficial for increasing the specific surface area of the electrode to reduce the local current density, thereby effectively delaying the triggering of dendrites.[26]

The regulation of lithium deposition behavior by the DNA interface layer stems from its unique chemical structure, where bases can act as Lewis bases to form stable coordination bonds with Li^+ (Lewis acid).[27] This transient Li–N/Li–O interaction reduces the diffusion barrier of Li^+, while the negatively charged phosphate backbone constructs an electrostatic field that attracts cations and repels anions, thereby significantly increasing the transference number of lithium ions. The lithium deposition morphologies on two different substrates, bare Cu and Cu@DNA, were compared *via* surface and cross-sectional SEM in Fig. 4(a)–(d). As seen in Fig. 4(a), after depositing a lithium areal capacity of 3 mAh cm^{-2} at a current density of 1 mA cm^{-2}, the bare copper surface exhibits uneven electric field distribution due to the "tip effect". Lithium deposition presents a loose, porous, needle-like dendrite structure, leading to severe volume expansion and the generation of a large amount of "dead lithium". This structure, with severe volume expansion, easily pierces the separator and triggers micro-short circuits.[6,28] In contrast, as observed in Fig. 3(b), on the Cu@DNA electrode surface, lithium ions achieve ordered nucleation

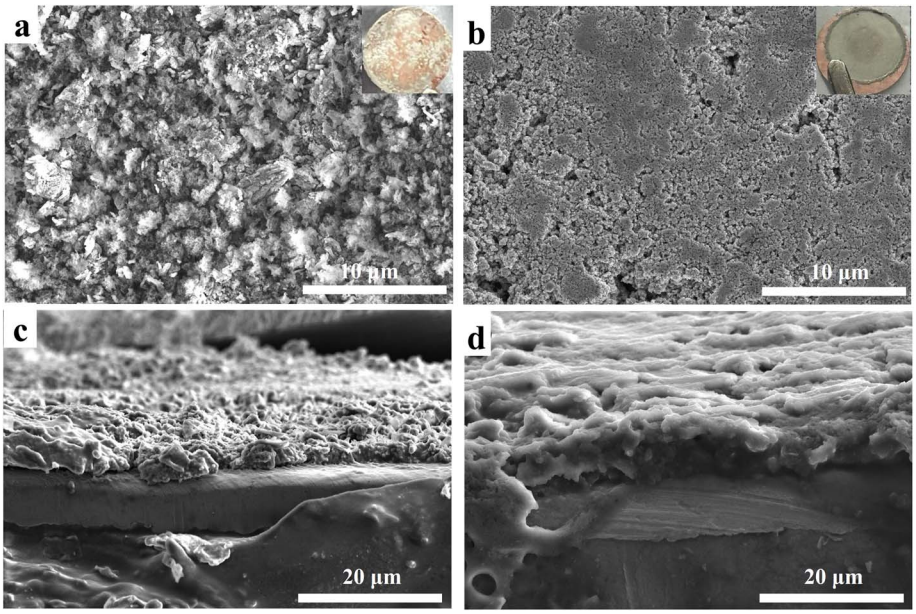

Fig. 4 Top view SEM images of Li deposited on (a) bare Cu and (b) Cu@DNA electrodes after plating 3 mAh cm^{-2} at 1 mA cm^{-2}. Cross sectional SEM images of (c) bare Cu and (d) Cu@DNA electrodes corresponding to the states in (a) and (b).

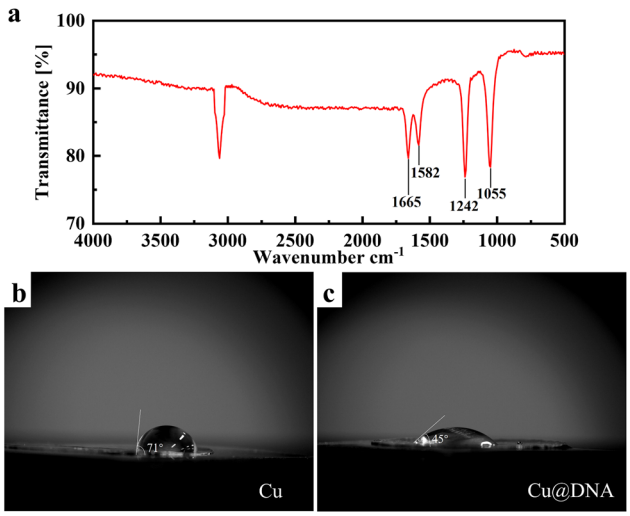

Fig. 5 (a) Fourier-transform infrared (FTIR) spectroscopy of Cu@DNA. (b) Contact angle test on bare Cu; (c) contact angle test on Cu@DNA.

under the guidance of DNA molecular channels. The deposition layer presents a dense, smooth, granular packing with no obvious dendrite formation. The circular magnified images in the upper right corners of Fig. 4(a) and (b) further confirm the significant difference in deposition behavior, where the bare copper electrode surface appears dull, rough, and lusterless, indicating the accumulation of a large amount of loose dead lithium and dendrites, causing severe light scattering. Conversely, the Cu@DNA electrode surface maintains a flat, uniform, and bright metallic luster after deposition, intuitively reflecting the dense lithium deposition behavior induced by the DNA interface layer, which effectively inhibits surface pulverization and dead lithium generation. For the bare copper electrode, due to the lack of effective interface regulation, lithium ions tend to undergo uncontrollable vertical growth, resulting in a loose, porous, and chaotic stacking state of the deposition layer, as shown in Fig. 4(c). This disordered growth leads to severe volume expansion and massive "dead lithium" generation, causing the contact between the deposition layer and the substrate to become loose or even peel off. In comparison, Fig. 4(d) clearly displays the two-dimensional layered deposition mode induced by the Cu@DNA electrode, which is dense and flat, tightly combined with the copper substrate, and no obvious pores or dendrites are observed. This morphological structure can effectively dissipate local mechanical stress during the deposition process and inhibit volume expansion, thereby maintaining the long-term integrity of the electrode structure. It also confirms the excellent "molecular buffering" capability of the DNA interface layer.

To explore the interaction mechanism between DNA molecules, the copper substrate, and lithium ions, Fourier transform infrared spectroscopy (FTIR) analysis was conducted, as shown in Fig. 5(a). The strong absorption peak at 1242 cm^{-1} is attributed to the asymmetric stretching vibration of the P=O bond in the DNA phosphate backbone. The characteristic peak at 1055 cm^{-1} corresponds to the skeletal vibration of C–O–C/P–O–C.[29] These phosphate groups (PO_4^{-3}) carry a high density of negative charges and can serve as "electrostatic potential wells" to pre-concentrate Li^+ at the interface, thereby constructing efficient ion transport channels.[30] Additionally, characteristic signals derived from DNA base pairs were observed in the 1500–1700 cm^{-1} region. Among them, the peak at 1582 cm^{-1} is assigned to the stretching vibration of the C=N bond and the planar bending vibration of N–H in the purine/pyrimidine rings, while the peak at 1665 cm^{-1} corresponds to the stretching vibration of C=O in guanine (G) and thymine (T). Polar

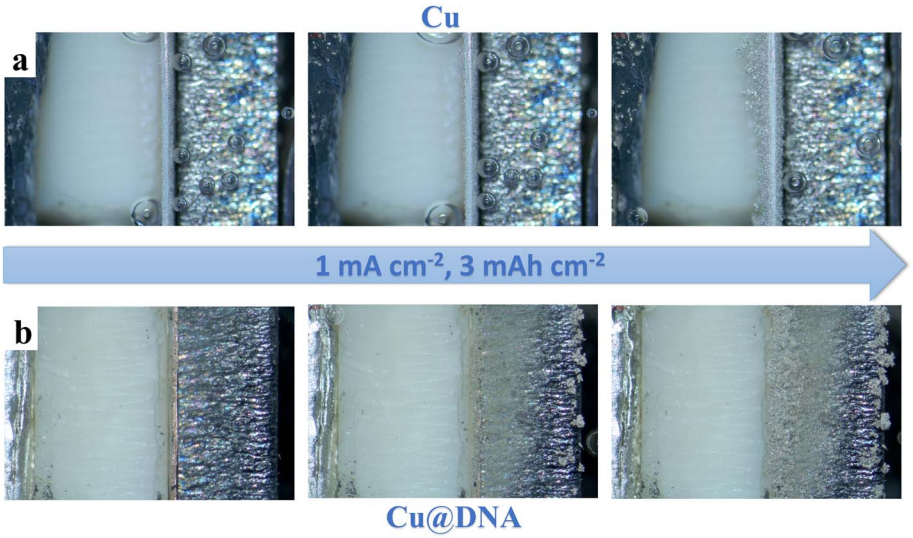

Fig. 6 *In situ* optical microscopy observations of Li dendrite growth at a current density of 1.0 mA cm^{-2} with a fixed areal capacity of 3.0 mAh cm^{-2}. (a) Morphology evolution on the bare Cu surface and (b) on the Cu@DNA surface during the Li plating process.

groups like C=O, C=N, and N–H in the DNA molecule are rich in lone-pair electrons. Within these groups, the N and O atoms serve as especially critical lithiophilic sites for binding lithium. Therefore, they effectively reduce the desolvation energy barrier of Li^+ by forming transient Li–N and Li–O coordination bonds, inducing uniform nucleation and two-dimensional layered deposition of lithium.[21] Although directly capturing such transient coordination dynamically during battery operation remains technically challenging, extensive spectroscopic evidence (*e.g.*, XPS and Raman) from recent studies on similar nitrogen-rich biopolymers and DNA-based interphases has consistently confirmed the strong binding between and pyridine/pyrrole-like nitrogen sites in nucleobases.[31–33] This literature consensus perfectly aligns with our DFT calculations and FTIR shifts, solidly validating that the base pairs can act as effective lithiophilic sites to regulate directional ion transport. By virtue of coordination effects, these electron-rich polar functional groups firmly anchor the DNA to the copper surface, simultaneously enhancing the wettability of the interface. As excellent interfacial wettability is a key factor in reducing interfacial impedance and homogenizing ion flux, contact angle tests were further conducted, as shown in Fig. 5(b) and (c). The test results indicate that the contact angle of the electrolyte at the interface was measured to be 71° for bare copper, which significantly decreased to 45° for the Cu@DNA electrode. The significant reduction in contact angle intuitively reflects the effective regulation of the surface energy of the copper substrate by DNA molecules, transforming it from a "lyophobic" to a "lyophilic" state. This superior lyophilicity helps accelerate the desolvation process of Li^+ (ref. 13) and promotes uniform infiltration of the electrolyte on the electrode surface, which is a prerequisite for achieving uniform lithium deposition.

To visually monitor the real-time dynamic growth behavior of lithium metal and verify the inhibitory effect of the DNA interface layer on dendrite growth, we assembled visualized transparent batteries and performed *in situ* optical microscopy characterization,[34] as shown in Fig. 6. During the electrochemical deposition process at a constant current density of 1 mA cm^{-2} and a deposition capacity of 3 mAh cm^{-2}, the morphological evolution of the electrode surface was recorded dynamically from left to right over time. For the bare copper electrode in Fig. 6(a), obvious local uneven nucleation can be observed at the initial stage of deposition. As the deposition time increases, due to the electric field concentration caused by the "tip effect", lithium preferentially grows rapidly at protrusions, causing the electrode surface to be quickly covered by loose, porous mossy and needle-like lithium dendrites. This uncontrolled growth mode easily punctures the separator, posing serious safety hazards. The deposition behavior of the Cu@DNA electrode in Fig. 6(b) is entirely different from Fig. 6(a). Benefiting from the uniform regulation of Li^+ flux by the lithiophilic sites of DNA molecules and the buffering effect of the phosphate backbone on the local electric field, the nucleation process of lithium ions is strictly confined within a two-dimensional plane. Throughout the deposition process, the electrode surface remains flat, dense, and smooth, without any obvious dendrite protrusions observed. These *in situ* observation results visually confirm the superior capability of the Cu@DNA biomimetic interface in inducing dendrite-free lithium deposition, which is highly consistent with the observations from Fig. 4(b) and (d).

To deeply reveal the regulation mechanism of the Cu@DNA biomimetic interface on ion transport kinetics and the SEI film evolution process, electrochemical impedance spectroscopy (EIS) were tested, with results shown in Fig. 7(a) and (b). Before testing, all batteries were rested for 10 hours to reach an equilibrium state. After the initial 10 cycles of testing, the SEI interface impedance of Cu@DNA is approximately 42 Ω, slightly lower than the 53 Ω of the bare copper SEI film. This indicates that in the initial cycles, although the contact state between the

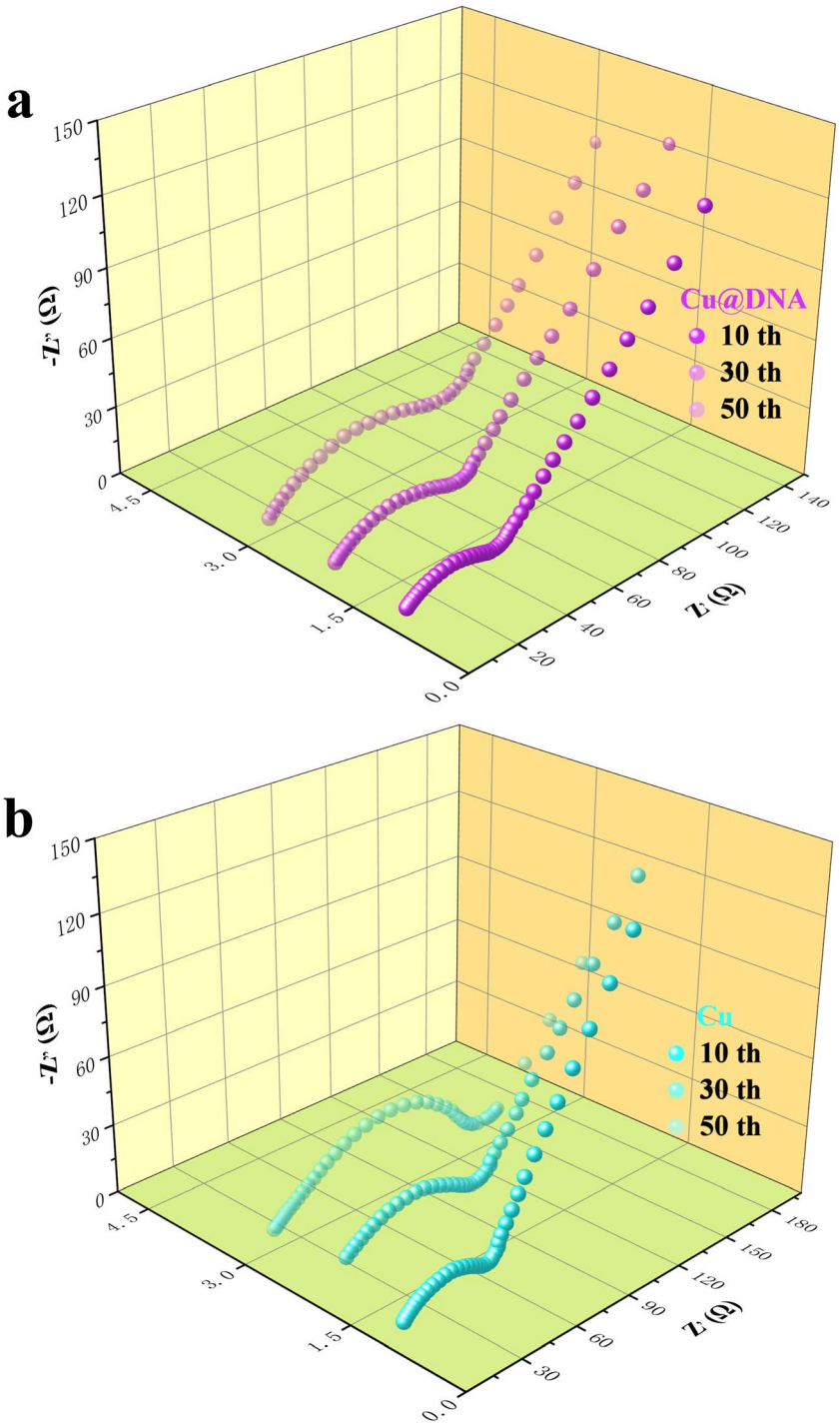

Fig. 7 Nyquist plots of the (a) Li|Cu@DNA half-cells after the 10th, 30th, and 50th cycles, (b) bare Li|Cu half-cells after the 10th, 30th, and 50th cycles.

two electrodes and the electrolyte is similar, the introduction of the DNA layer does not hinder ion transport. Instead, it reduces the interfacial transport impedance by virtue of its excellent ionic conductivity and accelerates the desolvation process of Li^+ using its abundant polar functional groups, thereby improving charge transfer kinetics.[7,35] As the number of cycles increases to 50, the impedance behaviors of the two diverge significantly. The resistance of the bare copper electrode increases sharply from 53 Ω to 135 Ω. This deterioration in impedance is attributed to the low surface energy of the copper substrate, which makes lithium ion nucleation difficult and prone to vertical dendrite growth patterns. Sharp lithium dendrites continuously pierce the SEI film, inducing new side reactions and generating a thick, high-resistance "dead lithium" layer, thereby

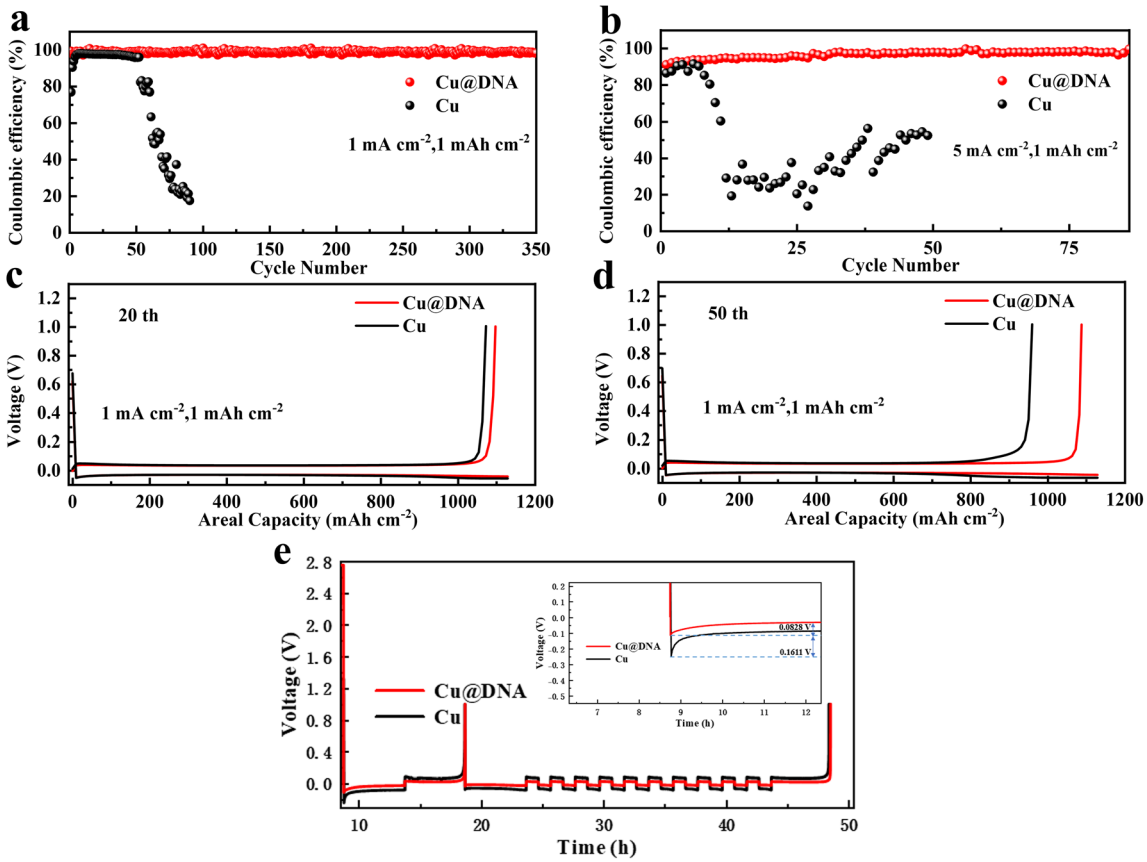

Fig. 8 Comparison of coulombic efficiencies between Cu@DNA and bare Cu electrodes at current densities of (a) 1.0 mA cm^{-2} and (b) 5.0 mA cm^{-2} with a fixed capacity of 1.0 mAh cm^{-2}. Galvanostatic discharge/charge voltage profiles at the (c) 20th cycle and (d) 50th cycle. (e) Detailed voltage profiles at 10 cycles.

significantly hindering interfacial kinetics. By contrast, after 50 cycles, the resistance of the Cu@DNA electrode increases only slightly from 42 Ω to 84 Ω, significantly lower than that of bare copper. This is mainly attributed to the abundant polar functional groups such as phosphate groups and bases in the DNA molecules, which effectively increase the surface energy of the copper substrate and improve the wettability of the interface. This modified interface can induce uniform deposition of lithium ions and effectively inhibit the vertical growth of dendrites, thereby enhancing overall electrochemical performance.[36,37]

2.4 Electrochemical performance analysis

2.4.1 Stability of half-cells and symmetric cells. Li|Cu half-cells were employed to evaluate the performance of Cu@DNA, as shown in Fig. 8(a). Under a test condition of 1 mA cm^{-2} current density, following a brief initial activation process, the coulombic efficiency (CE) of the Cu@DNA cell rapidly climbed to 99% and maintained long-term stability. It cycled stably for over 350 cycles. The bare copper cell showed a precipitous drop in CE after 60 cycles, indicating severe interfacial side reactions or short circuits caused by dendrites. The Cu@DNA electrode in Fig. 8(b) maintained a CE above 99% after 85 cycles even under a high current density of 5 mA cm^{-2}, demonstrating excellent rate tolerance. Fig. 8(c) and (d) show the capacity–voltage profiles of bare Cu and Cu@DNA electrodes at the 20th and 50th cycles under a current density of 1 mA cm^{-2}. The voltage polarization of the bare copper electrode expands markedly from the 20th to the 50th cycle due to SEI film thickening and rupture, which results from progressive dendrite growth and dead lithium accumulation. Conversely, the voltage curve of Cu@DNA after 50 cycles still highly overlaps with that of the 20th cycle. This superior electrochemical stability is attributed to the robust DNA biomimetic interface layer, which successfully inhibits side reactions and maintains the long-term integrity of the electrode interface. To visually confirm the excellent lithiophilicity of the Cu@DNA interface and its ability to reduce the lithium nucleation barrier, we conducted a 10-cycle test. As observed in Fig. 8(e), at the initial stage of lithium deposition, the Cu@DNA electrode exhibits a significantly reduced nucleation overpotential of only 0.0828 V, far lower than the 0.1611 V of bare copper. This advantage is attributed to the abundant lithiophilic functional groups in DNA molecules, such as phosphate groups and base nitrogen atoms, which effectively lower the crystallization barrier of Li^+ and induce rapid and uniform nucleation of lithium[38]

To evaluate the electrochemical stability of the Cu@DNA electrode during long-term repeated stripping/plating

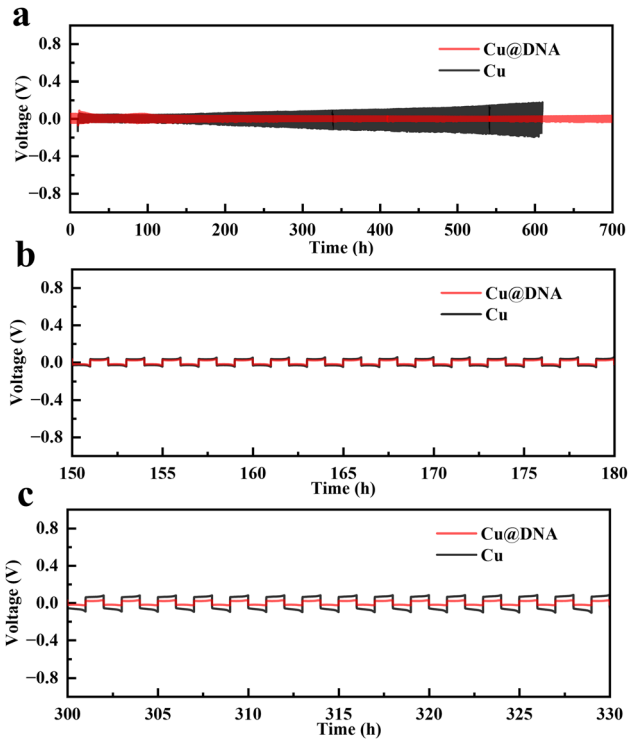

Fig. 9 Long-term interfacial stability evaluation. (a) Galvanostatic cycling performance of Li|Li symmetric cells assembled with Cu@DNA and bare Cu electrodes. Detailed voltage profiles showing the polarization evolution during the (b) 150–180th cycles and (c) 300–330th cycles.

processes, we assembled Li|Cu@DNA symmetric cells and performed tests, as shown in Fig. 9. As the uniform regulation of lithium flux by the DNA layer, the Li|Cu@DNA cell achieved ultra-stable stripping/plating cycles for up to 700 hours, with voltage hysteresis consistently maintained at a remarkably low level of 22 mV, as shown in Fig. 10(a). The Li|Cu symmetric cell exhibited pronounced voltage fluctuations after 200 hours, indicating interfacial instability caused by SEI film rupture and dendrite growth.[7] Fig. 9(b) and (c) are detailed magnified views of Fig. 9(a) at 150–180 hours and 300–330 hours. In Fig. 9(b), whether at 150–180 hours or 300–330 hours, the voltage curve of the Cu@DNA electrode always maintains a smooth, stable, and regular rectangular wave. The curve of Fig. 9(c) for bare copper typically exhibits chaotic fluctuations, voltage spikes, or significantly increased polarization. This further verifies the stabilizing effect of the biomimetic interface layer on the SEI film.[35]

2.4.2 Performance of coin full cells. To verify the preliminary practicality of this strategy, coin full cells using the Cu@DNA anode and NCM811 cathode were assembled. As shown in Fig. 10(a), at a 1C rate, the Cu@DNA|NCM811 cell exhibits excellent cycling stability, with a capacity retention rate as high as 92.7% after 300 cycles, far superior to the 66.3% of the bare copper system. Fig. 10(b) and (d) further compare the full cells galvanostatic charge–discharge voltage profiles at the 20th, 100th, and 200th cycles. It can be seen that the voltage curves in Fig. 10(b) of Cu@DNA|NCM811 have a high degree of overlap and slow specific capacity decay, demonstrating excellent electrochemical stability. Comparison with Cu|NCM811 in Fig. 10(d), as cycling progresses, the voltage curves show

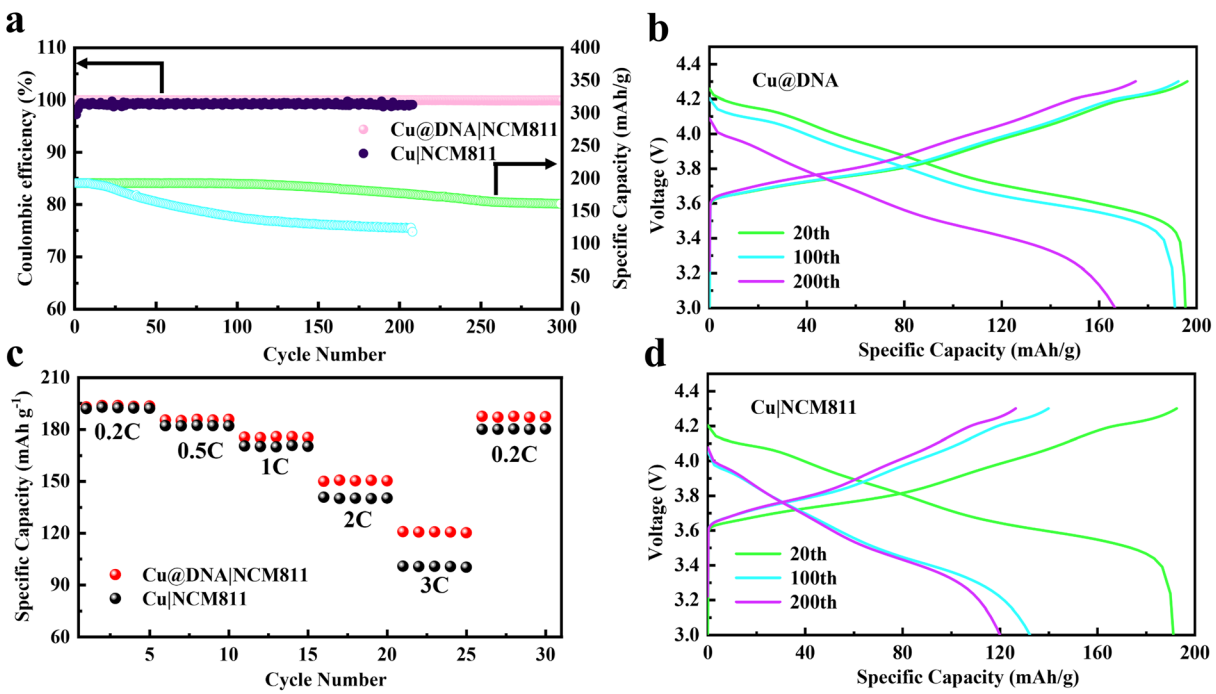

Fig. 10 Electrochemical performance of full cells paired with NCM811 cathodes. (a) Long-term cycling stability of Cu@DNA|NCM811 and bare Cu|NCM811 full cells at a rate of 1C. (b) Corresponding galvanostatic charge–discharge voltage profiles of the Cu@DNA|NCM811 cell at the 20th, 100th, and 200th cycles. (c) Rate capabilities of the two full cells tested at various C-rates. (d) Corresponding galvanostatic charge–discharge voltage profiles of the bare Cu|NCM811 cell at the 20th, 100th, and 200th cycles.

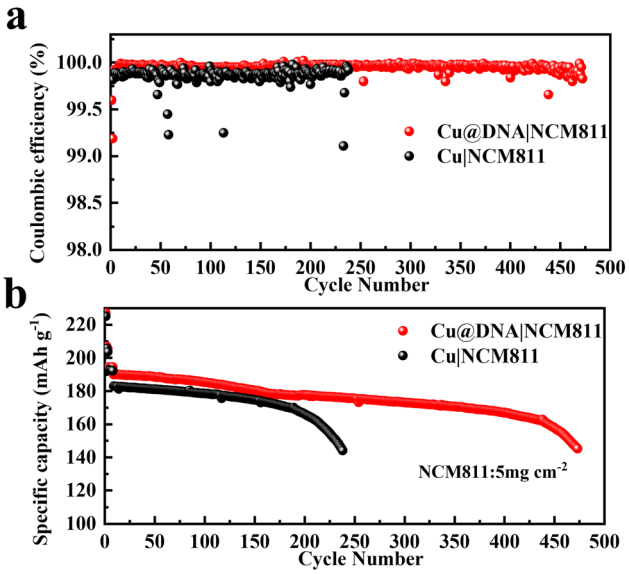

Fig. 11 Evaluation of Cu@DNA anodes in practical pouch cells. (a) coulombic efficiency of the Cu|NCM811 and Cu@DNA|NCM811 pouch cells at a rate of 0.5C. (b) Specific discharge capacity of the Cu|NCM811 and Cu@DNA|NCM811 pouch cells *versus* cycle number.

obvious capacity fading accompanied by aggravated polarization, confirming severe degradation of the bare copper interface during long-term cycling. As can be seen from the rate performance graph in Fig. 10(c), the discharge specific capacity of this cell maintains a high level within a wide rate range of 0.2C to 3C. Particularly at a high rate of 3C, the capacity is maintained at 130 mAh g^{-1}, whereas bare copper is only 93 mAh g^{-1}. This indicates that the DNA interface layer can still effectively maintain the integrity of the interface and inhibit polarization growth under high current operating conditions.[39,40]

2.4.3 Practical application verification in pouch cells. Given the superior performance exhibited by Cu@DNA in coin cells, to explore its application prospects in practical high specific energy devices, we assembled pouch cells based on the Cu@DNA composite anode and NCM811 cathode using a stacked structure to simulate the internal environment of actual industrial batteries Fig. 11(a) shows that the coulombic efficiency of the Cu|NCM811 pouch cell decays severely after 250 cycles, while Cu@DNA|NCM811 maintains a coulombic efficiency consistently close to 100% even over a long cycle life of 500 cycles, indicating that interfacial side reactions have been greatly inhibited.[41] This also directly proves that the DNA modification layer can still significantly enhance the charge/discharge reversibility of the battery under high loading and complex stress environments. To evaluate the capacity retention capability of the battery, harsh conditions with a cathode active material loading as high as 5 mg cm^{-2} were adopted, as shown in Fig. 11(b). The results show that the specific capacity of the Cu|NCM811 battery declines rapidly during cycling, and a dramatic capacity dive is observed after only 200 cycles, which is usually attributed to electrolyte dry-out and irreversible loss of active lithium.[24] By comparison, the specific capacity of the Cu@DNA|NCM811 pouch cell exhibits only slow, linear decay after 500 cycles, demonstrating excellent long-term cycling stability. Therefore, the introduction of a DNA modification layer on the copper substrate effectively solves the interface stability problem of pouch cells under large-size and high-loading conditions, significantly extending the long cycle life of Cu@DNA|NCM811 pouch cells, providing a practical and feasible technical strategy for anode interface modification compatible with high-loading cathodes.[14,16,42,43]

3 Conclusion

This study innovatively developed a biomimetic dual-functional interface layer Cu@DNA, based on natural strawberry DNA, and prepared lithium metal anode coin cells, half-cells, and full cells *via* a self-assembly process. Research indicates that DNA molecules, by virtue of their "molecular buffering" and "directional transport" dual effects, utilize the unique flexible chain structure of DNA to effective mitigate volume stress during the deposition process, enhancing the mechanical stability of the SEI film. Supported by DFT calculations, the phosphate backbone creates a deep electrostatic trap (−0.203 a. u.) and exhibits ultra-high binding energy (−7.13 eV) to act as a robust "molecular anchor" for Li^+ homogenization. Through the synergistic coordination effect of the phosphate backbone and bases, an energetic gradient is established where moderate-affinity bases (−2.77/−1.61 eV) facilitate efficient hopping conduction. Consequently, efficient Li^+ transport channels are constructed, achieving uniform nucleation and dense deposition of ions. The Cu@DNA anode not only achieved an ultra-high coulombic efficiency of 99.1% and a long cycle life of 700 hours in coin cells, performance that notably extends to 500 ultra-stable cycles in high-loading pouch cells. Beyond confirming the application potential of renewable biomass materials in the field of advanced energy storage, this work provides a highly promising biomimetic solution for solving the instability problem of metal anode interfaces.

Conflicts of interest

There are no conflicts to declare.

Data availability

The data that support the findings of this study are available from the corresponding author upon reasonable request.

Acknowledgements

This work was supported by the Scientific Research Startup Foundation of Guang'an Institute of Technology (Grant No. KYQD 2026 043, KYQD 2026 001), People's Republic of China.

References

1 J. Liu, Z. Bao, Y. Cui, E. J. Dufek, J. B. Goodenough, P. Khalifah, Q. Li, B. Y. Liaw, P. Liu, A. Manthiram, Y. S. Meng, V. R. Subramanian, M. F. Toney,

V. V. Viswanathan, M. S. Whittingham, J. Xiao, W. Xu, J. Yang, X.-Q. Yang and J.-G. Zhang, *Nat. Energy*, 2019, **4**, 180–186.
2 J. B. Goodenough and Y. Kim, *J. Power Sources*, 2011, **196**, 6688–6694.
3 W.-Z. Huang, P. Xu, X.-Y. Huang, C.-Z. Zhao, X. Bie, H. Zhang, A. Chen, E. Kuzmina, E. Karaseva, V. Kolosnitsyn, X. Zhai, T. Jiang, L.-Z. Fan, D. Wang and Q. Zhang, *MetalMat*, 2024, **1**, e6.
4 R. Tian, J. Jia, M. Zhai, Y. Wei, X. Feng, R. Li, J. Zhang and Y. Gao, *Heliyon*, 2024, **10**, e27181.
5 C. Fang, J. Li, M. Zhang, Y. Zhang, F. Yang, J. Z. Lee, M.-H. Lee, J. Alvarado, M. A. Schroeder, Y. Yang, B. Lu, N. Williams, M. Ceja, L. Yang, M. Cai, J. Gu, K. Xu, X. Wang and Y. S. Meng, *Nature*, 2019, **572**, 511–515.
6 D.-Y. Han, S. Kim, S. Nam, G. Lee, H. Bae, J. H. Kim, N.-S. Choi, G. Song and S. Park, *Adv. Sci.*, 2024, **11**, 2402156.
7 X. Wang, Z. Chen, X. Xue, J. Wang, Y. Wang, D. Bresser, X. Liu, M. Chen and S. Passerini, *Nano Energy*, 2025, **133**, 110439.
8 X.-Q. Zhang, X.-B. Cheng, X. Chen, C. Yan and Q. Zhang, *Adv. Funct. Mater.*, 2017, **27**, 1605989.
9 Y. Rao, X. Li, S. Zhao, P. Liu, F. Wu, X. Liu, N. Zhou, S. Fang and S. Passerini, *Nano Energy*, 2024, **123**, 109362.
10 S. Che and L. Fang, *Chem*, 2020, **6**, 2558–2590.
11 R. Xu, X.-B. Cheng, C. Yan, X.-Q. Zhang, Y. Xiao, C.-Z. Zhao, J.-Q. Huang and Q. Zhang, *Matter*, 2019, **1**, 317–344.
12 Y. Wang, Y. Zhang, Q. Zhang, X. Li, Q. Yan and Y. Zhu, *Adv. Sens. Energy Mater.*, 2024, **3**, 100113.
13 H. Zhao, Z. Wang, S. Yang, R. Zhang, J. Guo and D. Yang, *Biomaterials*, 2024, **309**, 122620.
14 S. B. Mitta, J. Kim, H. H. Rana, S. Kokkiligadda, Y. T. Lim, S. H. Bhang, H. S. Park and S. H. Um, *PNAS Nexus*, 2024, **3**, pgae213.
15 Z. Ouyang, Y. Wang, S. Wang, S. Geng, X. Zhao, X. Zhang, Q. Xu, B. Yuan, S. Tang, J. Li, F. Wang, G. Yao and H. Sun, *Adv. Mater.*, 2024, **36**, e2401114.
16 M. Yu, X. Tang, Z. Li, W. Wang, S. Wang, M. Li, Q. Yu, S. Xie, X. Zuo and C. Chen, *Chem. Soc. Rev.*, 2024, **53**, 4463–4489.
17 J. Tao, C. Zhang, X. Li, X. Chen, C. Ji, W. Wan and C. Wang, *J. Mater. Chem. A*, 2024, **12**, 18127–18136.
18 P. P. Edger, T. J. Poorten, R. VanBuren, M. A. Hardigan, M. Colle, M. R. McKain, R. D. Smith, S. J. Teresi, A. D. L. Nelson, C. M. Wai, E. I. Alger, K. A. Bird, A. E. Yocca, N. Pumplin, S. Ou, G. Ben-Zvi, A. Brodt, K. Baruch, T. Swale, L. Shiue, C. B. Acharya, G. S. Cole, J. P. Mower, K. L. Childs, N. Jiang, E. Lyons, M. Freeling, J. R. Puzey and S. J. Knapp, *Nat. Genet.*, 2019, **51**, 541–547.
19 H. Hirakawa, K. Shirasawa, S. Kosugi, K. Tashiro, S. Nakayama, M. Yamada, M. Kohara, A. Watanabe, Y. Kishida, T. Fujishiro, H. Tsuruoka, C. Minami, S. Sasamoto, M. Kato, K. Nanri, A. Komaki, T. Yanagi, Q. Guoxin, F. Maeda, M. Ishikawa, S. Kuhara, S. Sato, S. Tabata and S. N. Isobe, *DNA Res.*, 2014, **21**, 169–181.
20 B. Andrade, B. Dias, E. Silva, G. Santos and J. Lopes, *The Importance of Genetic Engineering in Modern Agriculture*, Seven Editora, 2024, ch. 10, pp. 44–52, DOI: 10.56238/sevened2024.010-044.
21 R. Zhang, X. R. Chen, X. Chen, X. B. Cheng, X. Q. Zhang, C. Yan and Q. Zhang, *Angew. Chem., Int. Ed. Engl.*, 2017, **56**, 7764–7768.
22 X. Chen, X. Chen and Q. Zhang, *ECS Meet. Abstr.*, 2020, **MA2020-01**, 869.
23 A. Pei, G. Zheng, F. Shi, Y. Li and Y. Cui, *Nano Lett.*, 2017, **17**, 1132–1139.
24 X. Tao, J. Wang, C. Liu, H. Wang, H. Yao, G. Zheng, Z. W. Seh, Q. Cai, W. Li, G. Zhou, C. Zu and Y. Cui, *Nat. Commun.*, 2016, **7**, 11203.
25 A. Pei, G. Zheng, F. Shi, Y. Li and Y. Cui, *Nano Lett.*, 2017, **17**, 1132–1139.
26 G. Zheng, S. W. Lee, Z. Liang, H.-W. Lee, K. Yan, H. Yao, H. Wang, W. Li, S. Chu and Y. Cui, *Nat. Nanotechnol.*, 2014, **9**, 618–623.
27 Y. Guo, H. Li and T. Zhai, *Adv. Mater.*, 2017, **29**, 1700007.
28 X. B. Cheng, R. Zhang, C. Z. Zhao and Q. Zhang, *Chem. Rev.*, 2017, **117**, 10403–10473.
29 M. Banyay, M. Sarkar and A. Gräslund, *Biophys. Chem.*, 2003, **104**, 477–488.
30 X. Cheng, M. Li, Y. Li, S. Song, S. Vallem and J. Bae, *ECS Meet. Abstr.*, 2024, **MA2024-01**, 350.
31 R. Zhang, X.-R. Chen, X. Chen, X.-B. Cheng, X.-Q. Zhang, C. Yan and Q. Zhang, *Angew. Chem., Int. Ed.*, 2017, **56**, 7764–7768.
32 Z. Ouyang, Y. Wang, S. Wang, S. Geng, X. Zhao, X. Zhang, Q. Xu, B. Yuan, S. Tang, J. Li, F. Wang, G. Yao and H. Sun, *Adv. Mater.*, 2024, **36**, 2401114.
33 Y. Gao, Z. Yan, J. L. Gray, X. He, D. Wang, T. Chen, Q. Huang, Y. C. Li, H. Wang, S. H. Kim, T. E. Mallouk and D. Wang, *Nat. Mater.*, 2019, **18**, 384–389.
34 K. N. Wood, E. Kazyak, A. F. Chadwick, K.-H. Chen, J.-G. Zhang, K. Thornton and N. P. Dasgupta, *ACS Cent. Sci.*, 2016, **2**, 790–801.
35 B. Peng, W. Bao, K. Sun and J. Xiao, *Enhancing Silicon Anode Performance in Lithium-Ion Batteries through Hybrid Artificial SEI Layer and Prelithiation*, 2025, DOI: 10.3390/nano15090690.
36 B. D. Adams, J. Zheng, X. Ren, W. Xu and J.-G. Zhang, *Adv. Energy Mater.*, 2018, **8**, 1702097.
37 S. Choi, T.-w. Kwon, A. Coskun and J. W. Choi, *Science*, 2017, **357**, 279–283.
38 K. Yan, Z. Lu, H.-W. Lee, F. Xiong, P.-C. Hsu, Y. Li, J. Zhao, S. Chu and Y. Cui, *Nat. Energy*, 2016, **1**, 16010.
39 H. Zhang, G. G. Eshetu, X. Judez, C. Li, L. M. Rodriguez-Martínez and M. Armand, *Angew. Chem., Int. Ed.*, 2018, **57**, 15002–15027.
40 Y. Zhang, W. Luo, C. Wang, Y. Li, C. Chen, J. Song, J. Dai, E. M. Hitz, S. Xu, C. Yang, Y. Wang and L. Hu, *Proc. Natl. Acad. Sci. U. S. A.*, 2017, **114**, 3584–3589.
41 T. Li, X.-Q. Zhang, P. Shi and Q. Zhang, *Joule*, 2019, **3**, 2647–2661.
42 P. Molaiyan, S. Bhattacharyya, G. S. dos Reis, R. Sliz, A. Paolella and U. Lassi, *Green Chem.*, 2024, **26**, 7508–7531.
43 Z. Wang, J. Wang, J. Ayarza, T. Steeves, Z. Hu, S. Manna and A. P. Esser-Kahn, *Nat. Mater.*, 2021, **20**, 869–874.